

# SCIENTIFIC REPORTS

OPEN

## The mechanism of charge density wave in Pt-based layered superconductors: SrPt<sub>2</sub>As<sub>2</sub> and LaPt<sub>2</sub>Si<sub>2</sub>

Received: 24 June 2015

Accepted: 10 September 2015

Published: 09 October 2015

Sooran Kim<sup>1</sup>, Kyoo Kim<sup>1,2</sup> & B. I. Min<sup>1</sup>

The intriguing coexistence of the charge density wave (CDW) and superconductivity in SrPt<sub>2</sub>As<sub>2</sub> and LaPt<sub>2</sub>Si<sub>2</sub> has been investigated based on the *ab initio* density functional theory band structure and phonon calculations. We have found that the CDW instabilities for both cases arise from the q-dependent electron-phonon coupling with quasi-nesting feature of the Fermi surface. The band structure obtained by the band-unfolding technique reveals the sizable q-dependent electron-phonon coupling responsible for the CDW instability. The local split distortions of Pt atoms in the [As-Pt-As] layers play an essential role in driving the five-fold supercell CDW instability as well as the phonon softening instability in SrPt<sub>2</sub>As<sub>2</sub>. By contrast, the CDW and phonon softening instabilities in LaPt<sub>2</sub>Si<sub>2</sub> occur without split distortions of Pt atoms. The phonon calculations suggest that the CDW and the superconductivity coexist in [X-Pt-X] layers (X = As or Si) for both cases.

Low-dimensional systems often suffer from intrinsic instabilities, revealing diverse interesting phase transitions upon cooling, such as charge density wave (CDW), spin density wave, superconductivity (SC), and so on. In general, those phases are detrimental to each other. Therefore the coexistence of those phases in a system has been a long-standing subject of importance in the physics of low-dimensional systems<sup>1–6</sup>. The Pt-based layered superconductors, SrPt<sub>2</sub>As<sub>2</sub> and LaPt<sub>2</sub>Si<sub>2</sub>, of the present study belong to such quasi two-dimensional (2D) systems, which exhibit the coexistence of the CDW and the SC at low temperature (*T*)<sup>7,8</sup>. In fact, the Pt-based layered systems draw recent attention because of their structural similarity to Fe-based AFe<sub>2</sub>As<sub>2</sub> (122) (A = Ba, Ca, Sr, or Eu) superconductors, which have been intensively studied these days<sup>9–17</sup>.

SrPt<sub>2</sub>As<sub>2</sub> was reported recently to be a BCS-like superconductor having two s-wave superconducting gap feature as in MgB<sub>2</sub><sup>18</sup>. SrPt<sub>2</sub>As<sub>2</sub> undergoes a CDW transition at  $T_{CDW} \approx 470$  K, which is accompanied by the superconducting transition at  $T_c \approx 5$  K. Below  $T_c$ , the SC coexists with the CDW phase<sup>7,19</sup>. At high *T*, SrPt<sub>2</sub>As<sub>2</sub> crystallizes in the tetragonal structure of CaBe<sub>2</sub>Ge<sub>2</sub>-type (*P4/nmm*), which is quite similar to ThCr<sub>2</sub>Si<sub>2</sub>-type structure of AFe<sub>2</sub>As<sub>2</sub> superconductors<sup>7</sup>. Differently from AFe<sub>2</sub>As<sub>2</sub>, however, Pt and As in SrPt<sub>2</sub>As<sub>2</sub> have reversed positions for every other layer, as shown in Fig. 1a. Namely, there are alternating [As2-Pt1-As2] and [Pt2-As1-Pt2] layers along the *c*-direction. The CDW modulation vector of SrPt<sub>2</sub>As<sub>2</sub> was reported experimentally to be  $q_{CDW} = 0.62 a^* = (0.62, 0, 0)$ , which yields the supercell structure with the modulation in the [As2-Pt1-As2] layers below  $T_{CDW}$  (see Fig. 4)<sup>19–21</sup>. Here  $a^*$  is the reciprocal lattice vector,  $a^* = (1, 0, 0)2\pi/a$ . Even below  $T_{CDW}$ , SrPt<sub>2</sub>As<sub>2</sub> has unique feature containing the split-off positions of Pt1 and As2, as shown in Fig. 1b. Interestingly, another CDW was recently observed at 255 K in [Pt2-As1-Pt2] layer too<sup>22</sup>.

There have been only a few band structure calculations for SrPt<sub>2</sub>As<sub>2</sub><sup>23,24</sup>. Nekrasov *et al.*<sup>23</sup> obtained the density of states (DOS) and Fermi surface (FS) of the high *T* phase of SrPt<sub>2</sub>As<sub>2</sub> having the tetragonal

<sup>1</sup>Department of Physics, Pohang University of Science and Technology, Pohang, 790-784, Korea. <sup>2</sup>c\_CCMR, Pohang University of Science and Technology, Pohang 790-784, Korea. Correspondence and requests for materials should be addressed to K.K. (email: [kyoo@postech.ac.kr](mailto:kyoo@postech.ac.kr)) or B.I.M. (email: [bimin@postech.ac.kr](mailto:bimin@postech.ac.kr))

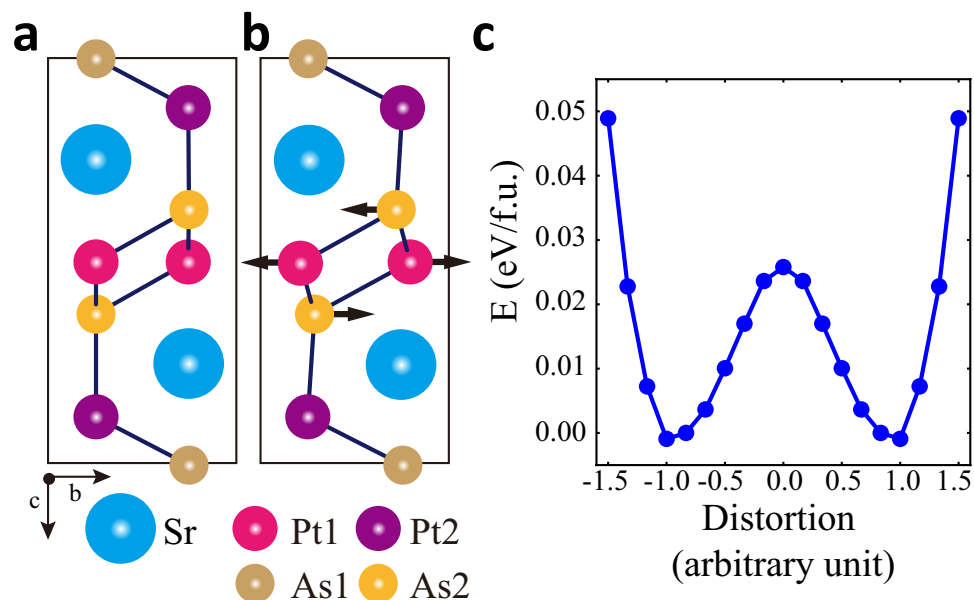


**Figure 1.** (a) Orthorhombic structure of SrPt<sub>2</sub>As<sub>2</sub> with Pt1 and As2 at the ideal positions without the split distortion (no-split-SPA). (b) Orthorhombic structure of SrPt<sub>2</sub>As<sub>2</sub> with Pt1 and As2 at the split-off positions (split-SPA). Black arrows in (b) represent the split distortions of Pt1 and As2. (c) Total energy variation of SrPt<sub>2</sub>As<sub>2</sub> with respect to the split distortion (distortion = 0.0 for no-split-SPA and distortion = 1.0 for split-SPA).

structure above  $T_{CDW}$ . They found that  $5d_{x^2-y^2}$  state of Pt1 is dominant at the Fermi level ( $E_F$ ) and the FSs are mostly 3D-like except one cylinder-like FS. Shein *et al.*<sup>24</sup> investigated the energetics of three types of 122 system: CaBe<sub>2</sub>Ge<sub>2</sub>-type and two hypothetical ThCr<sub>2</sub>Si<sub>2</sub>-type structures. They reported that CaBe<sub>2</sub>Ge<sub>2</sub>-type is more stable than ThCr<sub>2</sub>Si<sub>2</sub>-type polymorphs. However, none of these studies explored the electronic structures of the low  $T$  phase of SrPt<sub>2</sub>As<sub>2</sub> having the split-off positions of Pt and the CDW modulated structure.

Another Pt-based layered system LaPt<sub>2</sub>Si<sub>2</sub> has similar physical properties to SrPt<sub>2</sub>As<sub>2</sub>. At high  $T$ , LaPt<sub>2</sub>Si<sub>2</sub> crystallizes in the tetragonal structure of CaBe<sub>2</sub>Ge<sub>2</sub>-type, which is similar to Fig. 1a (Sr and As are replaced by La and Si). Upon cooling, it undergoes the CDW transition at 112 K with the CDW vector of  $q_{CDW} = (n/3, 0, 0)$  ( $n = 1$  or  $2$ )<sup>8</sup>. Nagano *et al.*<sup>8</sup> suggested a CDW-induced supercell at low  $T$ , which corresponds to the tripling of the original unit cell. Below  $T \sim 2$  K, the SC emerges in coexistence with the CDW state<sup>8</sup>. It was also reported that LaPt<sub>2</sub>Si<sub>2</sub> is more stable in the CaBe<sub>2</sub>Ge<sub>2</sub>-type structure than in the ThCr<sub>2</sub>Si<sub>2</sub>-type structure<sup>25</sup>. The FSs of CaBe<sub>2</sub>Ge<sub>2</sub>-type structure are mostly 2D-like, while the FSs of ThCr<sub>2</sub>Si<sub>2</sub>-type structure are 3D-like. However, the unique feature of the split-off positions of Pt1 and As2 in SrPt<sub>2</sub>As<sub>2</sub> has not been observed in LaPt<sub>2</sub>Si<sub>2</sub>.

Despite existing studies on SrPt<sub>2</sub>As<sub>2</sub> and LaPt<sub>2</sub>Si<sub>2</sub>, there are important remaining issues. There has been no theoretical explanation on the mechanisms of the observed CDW instabilities in SrPt<sub>2</sub>As<sub>2</sub> and LaPt<sub>2</sub>Si<sub>2</sub>. Kudo *et al.*<sup>7</sup> once stated that the CDW transition of SrPt<sub>2</sub>As<sub>2</sub> seemed to originate from the FS nesting, but they did not specify which band is responsible for the FS nesting. Above all, it has not been clarified whether the CDW instabilities in SrPt<sub>2</sub>As<sub>2</sub> and LaPt<sub>2</sub>Si<sub>2</sub> have the same mechanisms or not. Also, there have been no phonon studies on SrPt<sub>2</sub>As<sub>2</sub> and LaPt<sub>2</sub>Si<sub>2</sub>, which can provide direct clue to the CDW structural transitions. On the basis of phonon studies, one can also investigate SC properties in these CDW systems.

In this letter, to address the above questions, we have investigated the CDW and SC properties of SrPt<sub>2</sub>As<sub>2</sub> and LaPt<sub>2</sub>Si<sub>2</sub>, using the first-principles density-functional theory (DFT) band structure and phonon calculations. In SrPt<sub>2</sub>As<sub>2</sub>, the split distortions of Pt1 in [As2-Pt1-As2] layers are found to play an essential role in driving the CDW instability. This feature in SrPt<sub>2</sub>As<sub>2</sub> is distinct from that in LaPt<sub>2</sub>Si<sub>2</sub> that does not need the split distortions to drive the CDW instability. However, the  $\mathbf{q}$ -dependent electron-phonon interaction with quasi-nesting feature of the FS is expected to drive the CDW transitions in both cases. The phonon studies also revealed that the SC emerges mainly in the CDW layer of Pt1 for both SrPt<sub>2</sub>As<sub>2</sub> and LaPt<sub>2</sub>Si<sub>2</sub>.

## Results

To examine the mechanism of CDW instability in SrPt<sub>2</sub>As<sub>2</sub>, we focused on the role of split distortions of Pt, and so considered two structures. The first one is the orthorhombic structure in Fig. 1a without

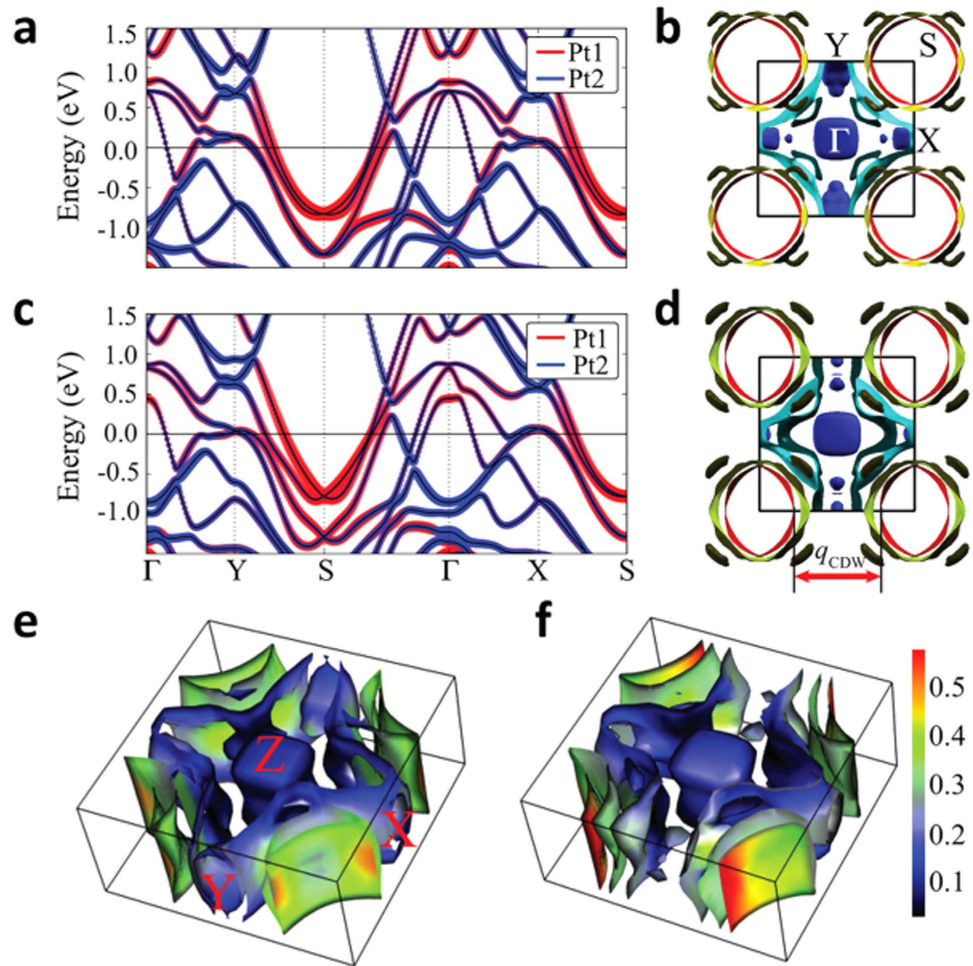


**Figure 2.** (a) Band structure of no-split-SPA. Pt1 and Pt2 band characters are shown with fat bands. (b) FS of no-split-SPA in the  $a^*b^*$  plane. (c) Band structure of split-SPA. (d) FS of split-SPA in the  $a^*b^*$  plane. The red FSs centered at S become flatter, which provides the nesting vector  $q_{CDW}$ . (e) FS of no-split-SPA in the full Brillouin zone (BZ). (f) FS of split-SPA in the full BZ. Color bar for (e,f) represents the Pt1 contribution to the FS (maximum value = 1). For split-SPA, the flat-red region is seen to be enhanced at the S-centered FSs.

the split distortions of Pt1 and As2 (we call it “no-split-SPA” hereafter). The no-split-SPA structure is close to the tetragonal  $\text{CaBe}_2\text{Ge}_2$ -type structure above  $T_{CDW}$ . The second one is another orthorhombic structure in Fig. 1b, which has the split-off positions of Pt1 and As2 (hereafter “split-SPA”). Split-SPA has the structure that is close to that of  $\text{SrPt}_2\text{As}_2$  below  $T_{CDW}$ , but does not contain the modulation by  $q_{CDW} = 0.62a^*$ . The split-SPA structure is obtained by making the antiferro-like distortions of Pt1 and As2 and then performing the atomic relaxation. The initial structure data for  $\text{SrPt}_2\text{As}_2$  before the structural relaxation was adopted from Imre *et al.*<sup>20</sup>. The initial lattice constant and atomic positions of  $\text{LaPt}_2\text{Si}_2$  were adopted from Shelton *et al.*<sup>26</sup>, and Nekrasov *et al.*<sup>23</sup>, respectively. The relaxed structural parameters of  $\text{SrPt}_2\text{As}_2$  and  $\text{LaPt}_2\text{Si}_2$  are summarized in the supplement<sup>27</sup>.

First, we checked the energetics of  $\text{SrPt}_2\text{As}_2$  with respect to the split distortion. The total energy variation from no-split-SPA to split-SPA is shown in Fig. 1c. The negative distortion means the opposite split directions of Pt1 and As2. We obtained the double-well shaped energy profile, which indicates that the split distortions of Pt1 and As2 indeed lower the total energy. The energy difference between no-split-SPA and split-SPA is  $\Delta E \approx 27 \text{ meV/f.u.}$

Figure 2 shows band structures and FSs of no-split-SPA and split-SPA. As shown in Fig. 2a,c, the main character of the dispersive bands around S is attributed to Pt1 band in both no-split-SPA and split-SPA. But the significant difference between the no-split-SPA and split-SPA is revealed in the FSs. Figure 2b,e for no-split-SPA show mainly the 3D-like FSs except one cylinder-like FS centered at S (red-colored FS in Fig. 2b), as is consistent with existing calculations<sup>23,24</sup>. Interestingly, the circular-cylindrical FS for no-split-SPA is changed into the ellipsoidal-cylindrical FS for split-SPA, as shown in Fig. 2d, and so the parallel portion of the FS is increased. Pt1-projected FSs of no-split-SPA and split-SPA are presented in Fig. 2e,f, respectively. For no-split-SPA, the FS has almost 4-fold rotational symmetry, and the Pt1

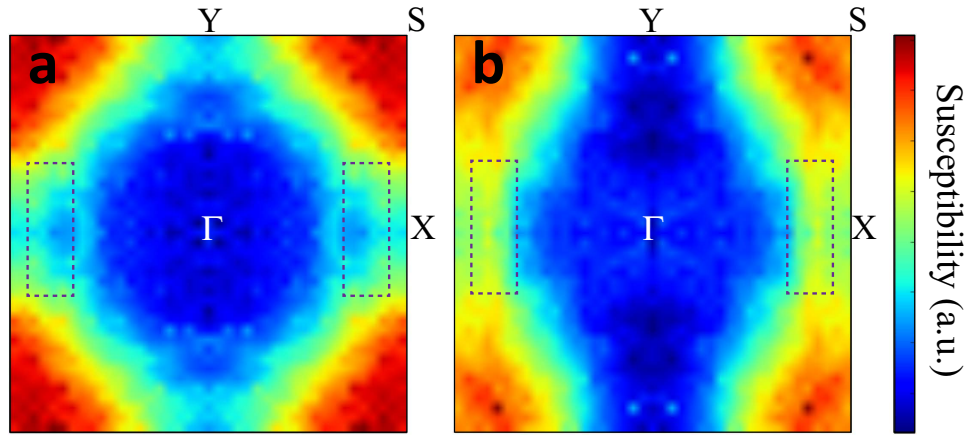


**Figure 3.** The projected charge susceptibility calculated with Pt1 matrix element for (a) no-split-SPA and (b) split-SPA. Dotted boxes represent the regimes of the observed CDW modulation vector  $q_{CDW}$  of SPA.

projection is distributed rather uniformly over the cylindrical FS. On the other hand, for split-SPA, the 4-fold rotational symmetry is completely broken because of the ellipsoidal-cylindrical FSs at S. It is worth noting in Fig. 2d that the nesting vector connecting the flat parts of ellipsoidal FSs is in good agreement with the experimental CDW modulation vector of  $q_{CDW} = (0.62, 0, 0)$  suggested by Imre *et al.*<sup>20</sup>. This result demonstrates that the split distortions of Pt1 and As2 in [As2-Pt1-As2] layer of split-SPA are essential to drive the CDW transition. Also notable feature in Fig. 2f is that the Pt1 character is dominant at longer parts of the ellipsoidal FSs, which clearly indicates that the Pt1 band is responsible for the CDW instability in split-SPA.

To check  $q_{CDW}$ , we have also calculated the charge susceptibility. The real part of charge susceptibility, however, does not show the pronounced peaks, which correspond to the observed CDW vector (Data are not shown). In fact, the discrepancy between the susceptibility peak and the experimental CDW vector has been previously pointed out<sup>28</sup>, which shows the limitation of bare susceptibility with a constant matrix element to predict a proper CDW vector. So, we have instead calculated the projected susceptibilities in Eq. 1 having the Pt1 matrix element, which is expected to give dominating contribution to the CDW transition:

$$\chi_0(\mathbf{q}) = - \sum_{\mathbf{k}\alpha\beta} \frac{f(\varepsilon_{\mathbf{k}\alpha}) - f(\varepsilon_{\mathbf{k}+\mathbf{q}\beta})}{\varepsilon_{\mathbf{k}\alpha} - \varepsilon_{\mathbf{k}+\mathbf{q}\beta}} A_{\mathbf{q}\alpha} A_{\mathbf{k}+\mathbf{q}\beta}, \quad (1)$$

where  $A_{\mathbf{k}\alpha}$  is the weight of a specific atom in the  $|\mathbf{k}\alpha\rangle$  wave function. This calculation method considers the special role of a specific atom in the present case, Pt1 atom<sup>28</sup>. Figure 3 shows the projected susceptibilities calculated with matrix element of Pt1 for (a) no-split-SPA and (b) split-SPA. It is seen that, only for the split-SPA, the susceptibility peak appears near the experimental  $q_{CDW}$  (denoted by the dotted box), which indicates the quasi-nesting feature<sup>28</sup>. However, there exist other  $q$ -vectors having more pronounced peaks. We believe that this is the limitation of the susceptibility calculation because the susceptibility cannot capture the electron-phonon interaction, which plays an important role in the CDW transition<sup>29–31</sup>.

In order to consider the electron-phonon interaction in the CDW transition, we performed phonon dispersion calculations for both no-split-SPA and split-SPA. As shown in Fig. 4a,b, the phonon softening instabilities occur in both cases, indicating the structural instabilities. This feature is consistent with experiment in that the ground state of SrPt<sub>2</sub>As<sub>2</sub> has the CDW modulated structure<sup>20</sup>. The softened phonon modes arise mainly from Pt1, as shown in the partial phonon DOSs, suggesting that the CDW transition occurs in the Pt1 layers. It also suggests that the Pt1 layer has the large electron-phonon interaction. Inset of Fig. 4a shows the normal mode of softened phonon at  $\Gamma$  for no-split-SPA, which induces the split distortions of Pt1 and As2. This phonon mode induces the structural transition from no-split-SPA to split-SPA, which is consistent with structural energetics in Fig. 1c.

Figure 4b shows that the  $\Gamma$  point softening disappears for split-SPA, and the phonon softening instability becomes dominant near  $(0.4, 0, 0)$ , which is equivalent to  $(0.6, 0, 0)$ . This value is consistent with the experimental  $q_{CDW} = (0.62, 0, 0)$ <sup>20</sup>. Indeed, the relaxed structure modulated by the softened phonon mode at  $\mathbf{q} = (0.6, 0, 0)$  in Fig. 4c is very close to the experimentally suggested structure after the CDW transition<sup>20</sup>. We will refer to this relaxed structure as 5X-SPA, as it is five-fold supercell structure due to  $\mathbf{q} = (0.6, 0, 0)$ . The total energy of 5X-SPA is lower than that of split-SPA by  $\sim 19$  meV/f.u. Figure 4d shows the unfolded band structure of 5X-SPA into the Brillouin zone (BZ) of the split-SPA. In comparison to Fig. 2c, the partial band gap opening appears along Y-S, as indicated by red circle. This partial gap

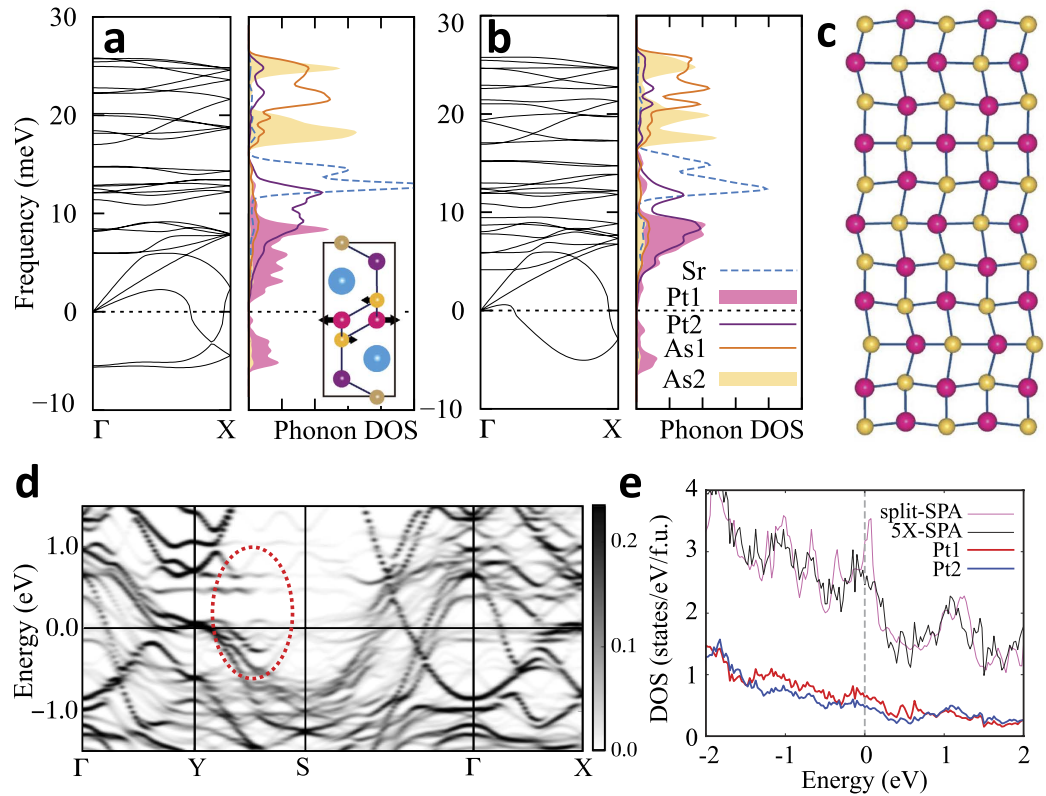


**Figure 4.** (a) Phonon dispersion and partial phonon DOS for no-split-SPA. (b) The same for split-SPA. The negative frequency here implies the imaginary phonon frequency, indicating the structural instability. In the inset of (a), the softened phonon mode at  $\Gamma$  is depicted. (c) The modulated structure (5X-SPA) of [As2-Pt1-As2] layer in the  $ab$  plane due to the softened phonon mode at  $\mathbf{q} = (0.6, 0, 0)$  of (b). (d) The band structure of 5X-SPA unfolded into the BZ of split-SPA. In comparison to band structures in Fig. 2c, the partial band gap opens along YS after the CDW transition (red-circled region). (e) Total electron DOSs are compared between the split-SPA and 5X-SPA cases. Partial electron DOSs of Pt1 and Pt2 of 5X-SPA are also plotted.

emerges due to the structural displacements modulated by the phonon mode at  $(0.6, 0, 0)$ . The significant change of the electronic structure by the phonon mode reveals the sizable electron-phonon interaction of that phonon mode. The partial gap opening along Y-S is indeed consistent with the band structure calculation in Fig. 2, confirming that the Pt1 band along Y-S is responsible for the CDW instability. Therefore, the combined study of electronic structure and phonon calculations demonstrates that the CDW of  $\text{SrPt}_2\text{As}_2$  originates from the  $\mathbf{q}$ -dependent electron-phonon coupling with quasi-nesting feature of the FS.

Figure 4e provides the total DOSs of split-SPA and 5X-SPA, which shows that 5X-SPA is still metallic, reflecting that the CDW nesting is imperfect. Only the partial gap opens with the modulation vector, as shown in Fig. 4d. This is one reason why the CDW and the SC could coexist in  $\text{SrPt}_2\text{As}_2$ <sup>1</sup>. The DOS at  $E_F$  ( $N(E_F)$ ) is lower for 5X-SPA (2.46 states/eV/f.u.) than for split-SPA (3.18 states/eV/f.u.). The calculated specific heat coefficient  $\gamma_{\text{cal}}$  for 5X-SPA is 5.80 mJ/molK<sup>2</sup>. Using the experimental specific heat coefficient  $\gamma_{\text{exp}} = 9.72$  mJ/molK<sup>2</sup><sup>7</sup>, the electron-phonon coupling constant  $\lambda$  of 0.68 is obtained from  $\gamma_{\text{exp}} = \gamma_{\text{cal}}(1 + \lambda)$ . This moderate coupling suggests that  $\text{SrPt}_2\text{As}_2$  would be a conventional BCS superconductor mediated by phonon<sup>24</sup>. Notable feature is that, even after the CDW transition, the contribution to the DOS at  $E_F$  comes more from Pt1 band. The ratio of Pt1 and Pt2 DOSs at  $E_F$  is  $\sim 1.3$ . This value would be enhanced with the consideration of the additional CDW at 255 K, which occurs in [Pt2-As1-Pt2] layer<sup>22</sup>. This indicates that the [As2-Pt1-As2] layer is more susceptible to the emergence of the SC.

For comparison, we performed the band structure and phonon calculations for tetragonal  $\text{LaPt}_3\text{Si}_2$  (t-LPS). Figure 5a shows the band structure of t-LPS. The Pt1 band produces the electron pocket FSs around M. The FS in red around M, which originates from Pt1 band, quite resembles two parallel FSs, as plotted by dotted lines in Fig. 5b. In this case, the FS nesting occurs through the vector connecting the corners, which perfectly nests both parallel FSs<sup>32</sup>. The nesting vector indicated in Fig. 5b is quite close to the observed  $q_{\text{CDW}} = (1/3, 0, 0)$ <sup>8</sup>. We have also calculated the charge susceptibility. Here too, the susceptibility with constant matrix elements does not show the peak at the experimental CDW vector (Data is not shown). By contrast, the projected susceptibility with Pt1 matrix element produces the peak

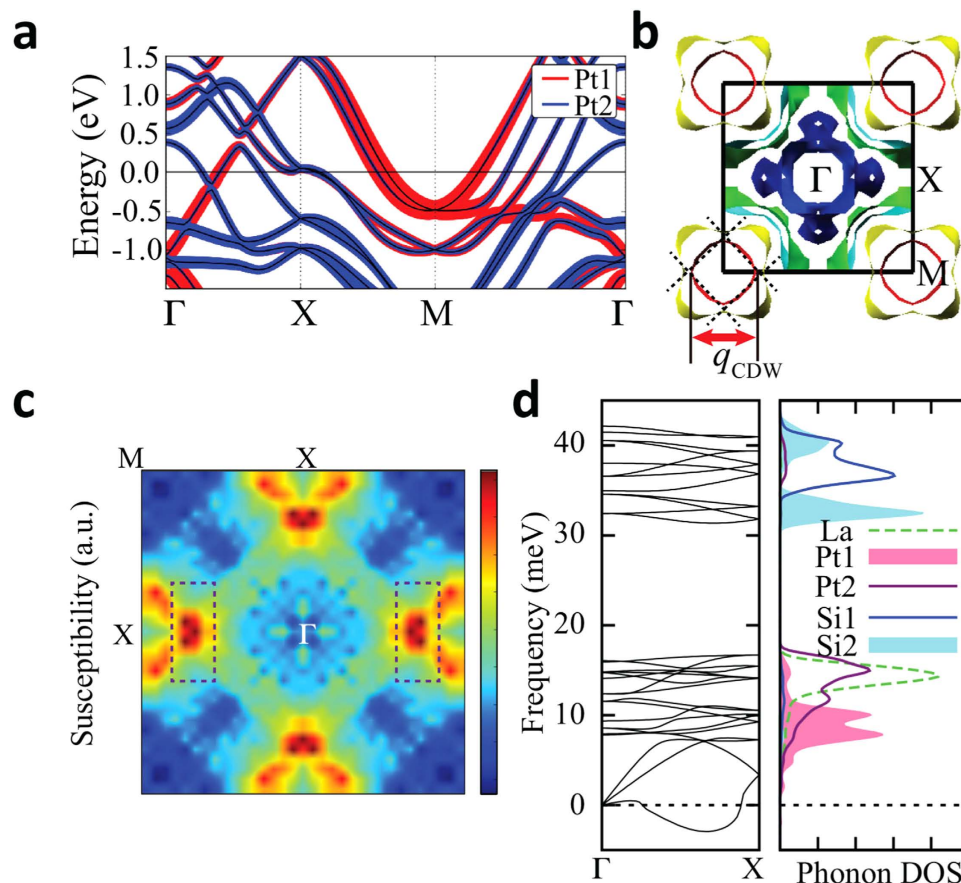


**Figure 5.** (a) Band structure of tetragonal  $\text{LaPt}_2\text{Si}_2$  (t-LPS). Pt1 and Pt2 band characters are shown with fat band. (b) FS of t-LPS. The nesting vector is close to the observed  $q_{\text{CDW}}$ . (c) The projected charge susceptibility with Pt1 matrix element for t-LPS. Dotted boxes represent the regimes of the observed CDW modulation vector  $q_{\text{CDW}}$  of LPS. (d) Phonon dispersion and partial phonon DOS of t-LPS.

near  $q_{\text{CDW}} = (1/3, 0, 0)$ , as denoted by the dotted box in Fig. 5c. The discrepancy between the total and projected susceptibilities implies again the quasi-nesting feature<sup>28</sup>.

To check the role of the electron-phonon coupling to structural transition, we have calculated the phonon dispersion curve of t-LPS too. The phonon dispersion of t-LPS in Fig. 5d contains the softened phonon mode, which is consistent with the CDW structural transition. The phonon softening occurs mainly from the Pt1, as in  $\text{SrPt}_2\text{As}_2$ , suggesting that the Pt1 layer has the large electron-phonon interaction. Therefore, the CDW instability in  $\text{LaPt}_2\text{Si}_2$  also arises from the  $\mathbf{q}$ -dependent electron-phonon coupling with quasi-nesting feature of the FS, as in  $\text{SrPt}_2\text{As}_2$ . But, in contrast to the case in  $\text{SrPt}_2\text{As}_2$ , the phonon softening at  $\Gamma$  causing the split distortions of Pt1 does not occur. It is compatible with the nonexistence of the split distortion in  $\text{LaPt}_2\text{Si}_2$ .

The difference between  $\text{LaPt}_2\text{Si}_2$  and  $\text{SrPt}_2\text{As}_2$  in the split distortions is expected to arise from the volume difference between  $\text{SrPt}_2\text{As}_2$  ( $100.08 \text{ \AA}^3/\text{f.u.}$ ) and  $\text{LaPt}_2\text{Si}_2$  ( $89.62 \text{ \AA}^3/\text{f.u.}$ ). To investigate the volume effect, the optimized atomic positions at each volume is determined by performing the structural relaxation calculations. Figure 6 shows the split distortion sizes of Pt1 and As2 (or Si2) as a function of volume. We found that the split distortions in  $\text{SrPt}_2\text{As}_2$  disappear with decreasing the volume as in Fig. 6a. In contrast, the split distortions appear in  $\text{LaPt}_2\text{Si}_2$  with increasing the volume as shown in Fig. 6b. These features suggest that stability of split distortions is strongly dependent on the volume of the system. Namely, the split distortions become stable with increasing the volume in both  $\text{SrPt}_2\text{As}_2$  and  $\text{LaPt}_2\text{Si}_2$ . We note another Pt-based superconductor,  $\text{BaPt}_2\text{Sb}_2$ , which also contains the deformed square lattice with the split-off Pt positions in [Sb-Pt-Sb] layer<sup>33</sup>. The volume of  $\text{BaPt}_2\text{Sb}_2$  is  $118.47 \text{ \AA}^3/\text{f.u.}$ , which is larger than those of  $\text{SrPt}_2\text{As}_2$  and  $\text{LaPt}_2\text{Si}_2$ .

The phonon softening instability at  $q = (1/3, 0, 0)$  is consistent with the observed CDW vector  $q_{\text{CDW}} = (1/3, 0, 0)$ , which produces the three-fold supercell structure. Figure 7(a) shows the relaxed structure generated by the softened phonon mode at  $q_{\text{CDW}} = (1/3, 0, 0)$ . We will refer to this structure as 3X-LPS. The total energy of 3X-LPS is lower than that of t-LPS by  $\sim 2 \text{ meV/f.u.}$  The modulations occur mainly in Pt1 layer of [Si2-Pt1-Si2], which suggests the Pt1 layer as the CDW layer, as in  $\text{SrPt}_2\text{As}_2$ . This

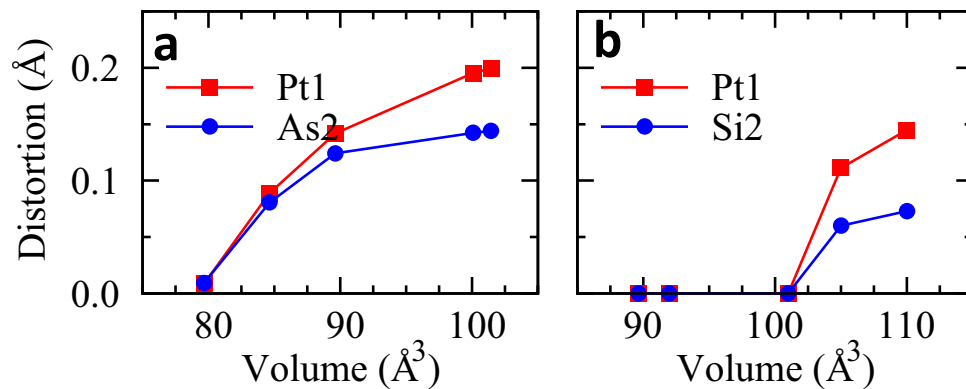


**Figure 6.** The variation of split distortion with the volume. (a) SrPt<sub>2</sub>As<sub>2</sub> (b) LaPt<sub>2</sub>Si<sub>2</sub>. The experimental volumes are 100.08 Å<sup>3</sup>/f.u. for SrPt<sub>2</sub>As<sub>2</sub> and 89.62 Å<sup>3</sup>/f.u. for LaPt<sub>2</sub>Si<sub>2</sub>.

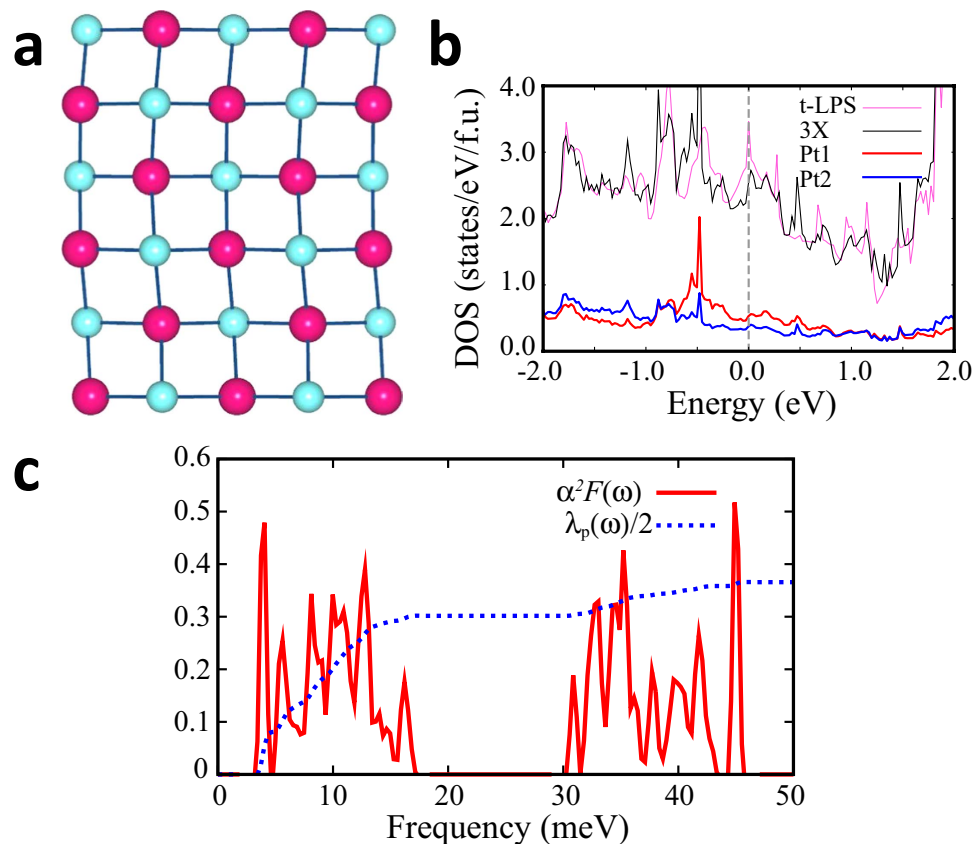


**Figure 7.** (a) The modified structure (3X-LPS) of [Si2-Pt1-Si2] layer in the *ab* plane due to the softened phonon mode at  $\mathbf{q} = (1/3, 0, 0)$ . (b) Total electron DOSs are compared between t-LPS and 3X-LPS. Partial electron DOSs of Pt1 and Pt2 of 3X-LPS are also plotted. (c) The Eliashberg function and  $\lambda_p(\omega)$  of 3X-LPS.

result is contrary to the speculation of Nagano *et al.*<sup>8</sup>, who claimed that [Pt2-Si1-Pt2] layer would be the CDW layer.

Figure 7(b) presents the DOSs of t-LPS and 3X-LPS. It is seen that 3X-LPS is still metallic even with the CDW distortion. The DOS at  $E_F$  is lower for 3X-LPS than for t-LPS, which is consistent with the stabilized 3X-LPS and also with the paramagnetic susceptibility measurement<sup>8</sup>. The ratio of Pt1 and Pt2 DOS at  $E_F$  for 3X-LPS is  $\sim 1.4$ . The higher DOS at  $E_F$  for Pt1 suggests that Pt1 layer is more susceptible to the SC transition.

To identify the main superconducting layer, we performed the calculation of e-ph coupling constant,  $\lambda_p$ , for 3X-LPS<sup>27</sup>. Figure 7(c) shows the Eliashberg function,  $\alpha^2F(\omega)$ , and the electron-phonon coupling constant,  $\lambda_p(\omega)$ , of 3X-LPS. The peak of  $\alpha^2F(\omega)$  and abrupt change of  $\lambda_p(\omega)$  appear at around  $\sim 3.9$  meV.

$N(E_F)$ (states/eV/f.u.)	$\omega_{log}$ (K)	$\Theta_D$ (K)	$\lambda_p$	$T_c$ (K) $\mu^* = 0.1, 0.13$
2.3	117.34	141.78	0.73	4.5, 3.5

**Table 1. Superconducting parameters of LaPt<sub>2</sub>Si<sub>2</sub>.**  $N(E_F)$ ,  $\omega_{log}$ , and  $\Theta_D$  are the DOS at  $E_F$ , the logarithmic average phonon frequency, and the Debye temperature, respectively.  $T_c$ 's are obtained for two effective Coulomb repulsion parameters  $\mu^* = 0.1$  and  $0.13$ .

Indeed this phonon frequency yields the largest contribution to  $\lambda_{qv}$  at  $q = \Gamma$ . The normal mode at this frequency is mainly composed of displacements of Pt1 in [Si2-Pt1-Si2] layer, which suggests that the main contribution to the SC comes from Pt1 layers. It is noteworthy that the Pt1 layer is the CDW-modulated layer, which implies that the SC and the CDW coexist in the same layer. The arrangement of Pt in [Si2-Pt1-Si2] layer is more 2D-like than in [Pt2-Si1-Pt2] layer. It is thus expected that the 2D nature and the CDW modulation of [Si2-Pt1-Si2] layer facilitate the emergence of the SC more effectively.

Finally, we have evaluated the superconducting parameters for 3X-LPS after the CDW transition, using the Eliashberg e-ph coupling theory and the Allen-Dynes formula for the critical temperature  $T_c$ <sup>34,35</sup>,

$$T_c = \frac{\omega_{log}}{1.20} \exp \left[ \frac{-1.04(1 + \lambda_p)}{\lambda_p(1 - 0.62\mu^*) - \mu^*} \right] \quad (2)$$

where  $\omega_{log} = \exp \left[ \frac{2}{\lambda_p} \int \frac{d\omega}{\omega} \alpha^2 F(\omega) \log \omega \right]$ ,  $\alpha^2 F(\omega)$  is the Eliashberg function, and  $\mu^*$  is the effective Coulomb repulsion parameter. As provided in Table 1, we have obtained  $T_c = 3.5$  K for  $\mu^* = 0.13$  ( $\mu^*$ : the effective Coulomb repulsion parameter), which is in good agreement with the observed  $T_c$  of  $\sim 2$  K<sup>8,26</sup>. Interestingly, the calculated electron-phonon coupling constant,  $\lambda_p$ , of 3X-LPS is comparable to experimentally estimated  $\lambda = 0.68$  of 5X-SPA, whose  $T_c \simeq 5$  K is close to  $T_c$  of LaPt<sub>2</sub>Si<sub>2</sub>.

## Conclusion

We have found that the CDW instabilities in both SrPt<sub>2</sub>As<sub>2</sub> and LaPt<sub>2</sub>Si<sub>2</sub> arise from the electron-phonon couplings with the quasi-nesting feature of the FSs. But the former takes place in the presence of the split distortions of Pt1 atoms, while the latter in the absence of the split distortions. These features are corroborated by the projected charge susceptibilities with Pt1 matrix element and the phonon softening instabilities at the observed CDW modulation vector of  $q_{CDW}$ . The unfolded band structure after the CDW transition in SrPt<sub>2</sub>As<sub>2</sub> reveals the sizable electron-phonon coupling of the relevant phonon mode. In both cases of SrPt<sub>2</sub>As<sub>2</sub> and LaPt<sub>2</sub>Si<sub>2</sub>, Pt1 band plays an essential role in the CDW and superconducting transitions, implying that the CDW and the SC coexist in the Pt1 layers.

## Methods

For the total energy band structure calculations, the full-potential linearized augmented plane wave band method implemented in Wien2k package was employed<sup>36</sup>. The generalized-gradient approximation (GGA) was used for the exchange correlation and the spin-orbit coupling (SOC) was included. For structural optimizations and phonon calculations, the pseudo-potential band method implemented in VASP<sup>37</sup> and phonopy<sup>38</sup> were used, respectively. The supercell approach with finite displacements based on the Hellmann-Feynman theorem<sup>39</sup> was used to obtain the force constants. The pseudo-potential band method implemented in Quantum Espresso was also used to determine the electron-phonon (e-ph) coupling constant  $\lambda_p$  and superconducting parameters<sup>40</sup>. The band-unfolding technique was employed to compare the band structures before and after the CDW modulation<sup>41,42</sup>.

## References

- Gabovich, A. M., Voitenko, A. I., Annett, J. F. & Ausloos, M. Charge- and spin-density-wave superconductors. *Supercond. Sci. Technol.* **14**, R1–R27 (2001).
- Kiss, T. *et al.* Charge-order-maximized momentum-dependent superconductivity. *Nat. Phys.* **3**, 720–725 (2007).
- Morosan, E. *et al.* Superconductivity in Cu<sub>x</sub>TiSe<sub>2</sub>. *Nat. Phys.* **2**, 544–550 (2006).
- Zhu, X., Lei, H. & Petrovic, C. Coexistence of Bulk Superconductivity and Charge Density Wave in Cu<sub>x</sub>ZrTe<sub>3</sub>. *Phys. Rev. Lett.* **106**, 246404 (2011).
- Machida, K. & Kato, M. Superconductivity transition temperature enhancement due to Peierls instability. *Phys. Rev. B* **36**, 854–856 (1987).
- Sangeetha, N. S. *et al.* Interplay of superconductivity and charge density wave ordering in pseudoternary alloy compounds: Lu<sub>2</sub>Ir<sub>2</sub>(Si<sub>1-x</sub>Ge<sub>x</sub>)<sub>5</sub>, Lu<sub>2</sub>(Ir<sub>1-x</sub>Rh<sub>x</sub>)<sub>2</sub>Si<sub>5</sub>, and (Lu<sub>1-x</sub>Sc<sub>x</sub>)<sub>2</sub>Ir<sub>2</sub>Si<sub>5</sub>. *Phys. Rev. B* **86**, 024524 (2012).
- Kudo, K., Nishikubo, Y. & Nohara, M. Coexistence of Superconductivity and Charge Density Wave in SrPt<sub>2</sub>As<sub>2</sub>. *J. Phys. Soc. Jpn.* **79**, 123710 (2010).
- Nagano, Y. *et al.* Charge Density Wave and Superconductivity of RPt<sub>2</sub>Si<sub>2</sub> (R = Y, La, Nd, and Lu). *J. Phys. Soc. Jpn.* **82**, 064715 (2013).
- Paglione, J. & Greene, R. L. High-temperature superconductivity in iron-based materials. *Nat. Phys.* **6**, 645–658 (2010).
- Stewart, G. R. Superconductivity in iron compounds. *Rev. Mod. Phys.* **83**, 1589–1652 (2011).



11. Torikachvili, M., Bud'ko, S., Ni, N. & Canfield, P. Pressure Induced Superconductivity in  $\text{CaFe}_2\text{As}_2$ . *Phys. Rev. Lett.* **101**, 057006 (2008).
12. Rotter, M., Tegel, M. & Johrendt, D. Superconductivity at 38 K in the Iron Arsenide  $(\text{Ba}_{1-x}\text{K}_x)\text{Fe}_2\text{As}_2$ . *Phys. Rev. Lett.* **101**, 107006 (2008).
13. Krellner, C. *et al.* Magnetic and structural transitions in layered iron arsenide systems:  $\text{AFe}_2\text{As}_2$  versus  $\text{RFeAsO}$ . *Phys. Rev. B* **78**, 100504 (R) (2008).
14. Kasinathan, D. *et al.*  $\text{AFe}_2\text{As}_2$  ( $A = \text{Ca}, \text{Sr}, \text{Ba}, \text{Eu}$ ) and  $\text{SrFe}_{2-x}\text{TM}_x\text{As}_2$  ( $\text{TM} = \text{Mn}, \text{Co}, \text{Ni}$ ): crystal structure, charge doping, magnetism and superconductivity. *New J. Phys.* **11**, 025023 (2009).
15. Takahashi, H. *et al.* High-Pressure Studies on Superconducting Iron-Based  $\text{LaFeAsO}_{1-x}\text{F}_x$ ,  $\text{LaFePO}$  and  $\text{SrFe}_2\text{As}_2$ . *J. Phys. Soc. Jpn.* **77**, Suppl. C 78–83 (2008).
16. Alireza, P. L. *et al.* Superconductivity up to 29 K in  $\text{SrFe}_2\text{As}_2$  and  $\text{BaFe}_2\text{As}_2$  at high pressures. *J. Phys. Condens. Matter* **21**, 012208 (2009).
17. Uhoja, W. *et al.* Anomalous compressibility effects and superconductivity of  $\text{EuFe}_2\text{As}_2$  under high pressures. *J. Phys. Condens. Matter* **22**, 292202 (2010).
18. Xu, X. *et al.* Evidence for two energy gaps and Fermi liquid behavior in the  $\text{SrPt}_2\text{As}_2$  superconductor. *Phys. Rev. B* **87**, 224507 (2013).
19. Fang, A. F. *et al.* Single-crystal growth and optical conductivity of  $\text{SrPt}_2\text{As}_2$  superconductors. *Phys. Rev. B* **85**, 184520 (2012).
20. Imre, A. *et al.* Inkommensurabel modulierte Kristallstrukturen und Phasenumwandlungen - Die Verbindungen  $\text{SrPt}_2\text{As}_2$  und  $\text{EuPt}_2\text{As}_2$ . *Z. Anorg. Allg. Chem.* **633**, 2037–2045 (2007).
21. The additional CDW modulation vector,  $q = 0.23 a^*$ , was recently reported by Wang, L. *et al.* Two-coupled structural modulations in charge-density-wave state of  $\text{SrPt}_2\text{As}_2$  superconductor. *Chinese Phys. B* **23**, 086103 (2014).
22. Kawasaki, S. *et al.* Coexistence of multiple charge-density waves and superconductivity in  $\text{SrPt}_2\text{As}_2$  revealed by  $^{75}\text{As}$ -NMR/NQR and  $^{195}\text{Pt}$ -NMR. *Phys. Rev. B* **91**, 060510 (R) (2015).
23. Nekrasov, I. A. & Sadovskii, M. V. Electronic structure of novel multiple-band superconductor  $\text{SrPt}_2\text{As}_2$ . *JETP Lett.* **92**, 751–755 (2010).
24. Shein, I. R. & Ivanovskii, A. L. Electronic band structure, Fermi surface, and elastic properties of polymorphs of the 5.2 K iron-free superconductor  $\text{SrPt}_2\text{As}_2$  from first-principles calculations. *Phys. Rev. B* **83**, 104501 (2011).
25. Hase, I. & Yanagisawa, T. Electronic structure of  $\text{LaPt}_2\text{Si}_2$ . *Physica C* **484**, 59–61 (2013).
26. Shelton, R. N., Braun, H. F. & Musick, E. Superconductivity and relative phase stability in 1:2:2 ternary transition metal silicides and germanides. *Solid State Commun.* **52**, 797–799 (1984).
27. See *Supplemental Material* for detailed structure parameters, the effect of the SOC in 3X-LPS.
28. Mazin, I. I.  $\text{Sr}_2\text{VO}_3\text{FeAs}$  as compared to other iron-based superconductors. *Phys. Rev. B* **81**, 020507 (R) (2010).
29. Eiter, H. *et al.* Alternative route to charge density wave formation in multiband systems. *Proc. Natl. Acad. Sci.* **110**, 64–69 (2013).
30. Zhu, X., Cao, Y., Zhang, J., Plummer, E. W. & Guo, J. Classification of charge density waves based on their nature. *Proc. Natl. Acad. Sci.* **112**, 2367 (2015).
31. Maschek, M. *et al.* Wave-vector-dependent electron-phonon coupling and charge-density-wave transition in  $\text{TbTe}_3$ . *Phys. Rev. B* **91**, 235146 (2015).
32. Yao, H., Robertson, J. A., Kim, E.-A. & Kivelson, S. A. Theory of stripes in quasi-two-dimensional rare-earth tellurides. *Phys. Rev. B* **74**, 245126 (2006).
33. Imai, M. *et al.* Superconductivity in 122-type antimonide  $\text{BaPt}_2\text{Sb}_2$ . *Phys. Rev. B* **91**, 014513 (2015).
34. Eliashberg, G. M. Zh. Eksp. Teor. Fiz. **38**, 966 (1960).
35. Allen, P. B. & Dynes, R. C. Transition temperature of strong-coupled superconductors reanalyzed. *Phys. Rev. B* **12**, 905–922 (1975).
36. Blaha, P., Schwarz, K., Madsen, G. K. H., Kvasnicka, D. & Luitz, J. *WIEN2K, An Augmented Plane Wave Plus Local Orbitals Program for Calculating Crystal Properties* (Vienna University of Technology, Austria, 2001).
37. Kresse, G. and Furthmüller, Efficient iterative schemes for ab initio total-energy calculations using a plane-wave basis set. *Phys. Rev. B* **54**, 11169 (1996).
38. Togo, A., Oba, F. & Tanaka, I. First-principles calculations of the ferroelastic transition between rutile-type and  $\text{CaCl}_2$ -type  $\text{SiO}_2$  at high pressures. *Phys. Rev. B* **78**, 134106 (2008).
39. Parlinski, K., Li, Z. Q. & Kawazoe, Y. First-Principles Determination of the Soft Mode in Cubic  $\text{ZrO}_2$ . *Phys. Rev. Lett.* **78**, 4063–4066 (1997).
40. Giannozzi, P. *et al.* QUANTUM ESPRESSO: a modular and open-source software project for quantum simulations of materials. *J. Phys. Condens. Matter* **21**, 395502 (2009).
41. Medeiros, P. V. C., Stafström, S. & Björk, J. Effects of extrinsic and intrinsic perturbations on the electronic structure of graphene: Retaining an effective primitive cell band structure by band unfolding. *Phys. Rev. B* **89**, 041407 (R) (2014).
42. Medeiros, P. V. C., Tsirkin, S. S., Stafström, S. & Björk, J. Unfolding spinor wave functions and expectation values of general operators: Introducing the unfolding-density operator. *Phys. Rev. B* **91**, 041116 (R) (2015).

## Acknowledgements

This work was supported by the NRF (Grant No. 2011-0025237), POSTECH BSRI grant, the National Creative Initiative (Grant No. 2009-0081576), Max-Planck POSTECH/KOREA Research Initiative (Grant No. KR 2011-0031558), and KISTI (Project No. KSC-2013-C3-065). We would like to thank Heejung Kim for helpful discussions.

## Author Contributions

K.K. and S.K. calculated and analyzed electronic structure and phonon data. S.K. wrote the manuscript. K.K. and B.I.M. supervised the work. All authors discussed the results and reviewed the manuscript.

## Additional Information

**Supplementary information** accompanies this paper at <http://www.nature.com/srep>

**Competing financial interests:** The authors declare no competing financial interests.

**How to cite this article:** Kim, S. *et al.* The mechanism of charge density wave in Pt-based layered superconductors:  $\text{SrPt}_2\text{As}_2$  and  $\text{LaPt}_2\text{Si}_2$ . *Sci. Rep.* **5**, 15052; doi: 10.1038/srep15052 (2015).



This work is licensed under a Creative Commons Attribution 4.0 International License. The images or other third party material in this article are included in the article's Creative Commons license, unless indicated otherwise in the credit line; if the material is not included under the Creative Commons license, users will need to obtain permission from the license holder to reproduce the material. To view a copy of this license, visit <http://creativecommons.org/licenses/by/4.0/>